Earth and Planetary Science Letters 553 (2021) 116637

Contents lists available at ScienceDirect

Earth and Planetary Science Letters

www.elsevier.com/locate/epsl

Convective tipping point initiates localization of basaltic fissure eruptions

Thomas J. Jones [a,b,*], Edward W. Llewellin [b]

[a] Department of Earth, Ocean and Ecological Sciences, University of Liverpool, Liverpool, L69 3GP, UK
[b] Department of Earth Sciences, Durham University, South Road, Durham, DH1 3LE, UK

ARTICLE INFO

Article history:
Received 5 April 2020
Received in revised form 3 September 2020
Accepted 14 October 2020
Available online 29 October 2020
Editor: H. Handley

Keywords:
exchange flow
excess degassing
eruption longevity
magma convection
Hawaiian eruptions

ABSTRACT

Basaltic fissure eruptions may evolve rapidly and unpredictably complicating hazard management. Localization of an elongate fissure to one or more focused vents may take days to months, and depends on fluid dynamic processes, such as thermally-driven viscous fingering, in the sub-volcanic plumbing system. However, fluid dynamics in a dyke geometry are poorly understood. We perform scaled analogue experiments to investigate convective magma exchange flow within a dyke-like conduit, and discover flow regimes ranging from chaotic mingling to stable, well-organized exchange, over the parameter space relevant for natural eruptions. Experiments are scaled via the Grashof number Gr, which is a Reynolds number for buoyancy-driven exchange flows. We propose that chaotic exchange at high Gr hinders thermally-driven localization by suppressing viscous fingering, whereas flow organization at low Gr enhances localization. Consequently, progressive decrease in Gr through increasing magma viscosity or decreasing dyke width pushes a fissure eruption towards a tipping point that results in rapid localization. Our findings indicate that current conceptual models for magma flow in a dyke require revision to account for this convective tipping point, and provide a quantitative framework for understanding the evolution of fissure eruptions.

1. Introduction

The fluid dynamics of magma ascent in the sub-volcanic plumbing system play a key role in determining the eruptive style of a volcano (Houghton et al., 2004). Basaltic fissure eruptions localize over time as a result of thermal (Bruce and Huppert, 1989) and thermo-rheological (Helfrich, 1995; Whitehead and Helfrich, 1991; Wylie et al., 1999) feedbacks – this phenomenon is of fundamental importance because it dictates the evolution of the eruptive hazard over time and space. Temperature perturbations along strike induce large variations in magma viscosity, leading to a viscous instability wherein flow focuses to regions of lower viscosity. However, the effect of in-conduit convection on flow localization has never been addressed. Here we investigate how convective flow patterns interact with thermo-rheological effects to enhance or hinder flow localization.

Multiple lines of evidence indicate that basaltic conduits commonly host density-driven convection, in which a lower-density upwelling magma exchanges with a higher-density downwelling magma (Fig. 1): (1) Excess SO_2 flux at persistently-active basaltic volcanoes indicates that magma ascends to the shallow conduit, outgasses, then descends without being erupted (Allard et al., 1994; Burton et al., 2007; Kazahaya et al., 1994; Oppenheimer et al., 2004; Palma et al., 2008; Stevenson and Blake, 1998; Witham, 2011). For example, data for the 1986-90 eruption of Izu-Oshima (Kazahaya et al., 1994), indicate a mean magma exchange flux of $\sim$3.4 m^3 s^{-1}, but a net eruption flux of only $\sim$0.2 m^3 s^{-1}. (2) Zonation in erupted crystals indicates that magma may repeatedly ascend and descend in the conduit (i.e. convect) before being recycled into magma at depth (Francalanci et al., 2012; Landi et al., 2008). (3) Lava has been directly observed to drain back down a fissure system during an eruption (e.g. 1974 eruption of Kīlauea; Wilson et al., 1995). (4) Concurrent upward and downward magma flow has been inferred from studies of flow textures in exposed vent deposits and dyke feeder systems at a range of depths (Geshi and Neri, 2014; Jones et al., 2017; Wadsworth et al., 2015).

The prevalence of in-conduit convective exchange has motivated an extensive body of experimental work to characterize and constrain the process (Beckett et al., 2014, 2011; Burton et al., 2007; Huppert and Hallworth, 2007; Kazahaya et al., 1994; Palma et al., 2011; Stevenson and Blake, 1998; Witham, 2011). However, all of the experimental work to date has assumed that ex-

* Corresponding author at: Department of Earth, Ocean and Ecological Sciences, University of Liverpool, Liverpool, L69 3GP, UK.
E-mail address: thomas.jones@liverpool.ac.uk (T.J. Jones).

https://doi.org/10.1016/j.epsl.2020.116637

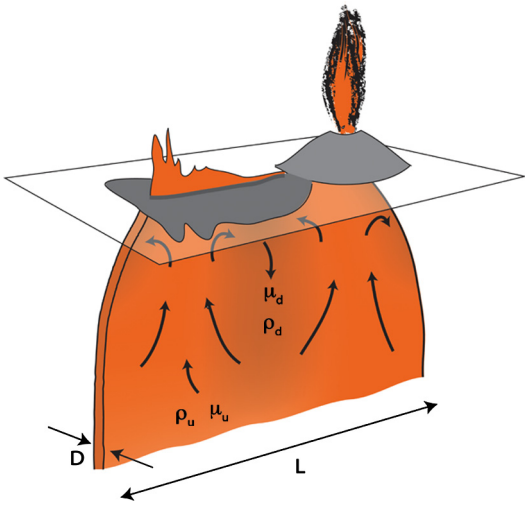

Fig. 1. Schematic of a basaltic fissure system wherein upwelling 'fresh' magma of lower density (ρ_u) and viscosity (μ_u) co-exists alongside downwelling magma of higher density (ρ_d) and higher viscosity (μ_d). The magma filled crack, or dyke, at depth has a width, D, and an along strike length, L.

change occurs in a cylindrical pipe, with the exception of Pioli et al. (2017), who investigate the ascent of bubble plumes in a slot geometry and give a qualitative description of associated marginal convection cells. Observed flow patterns in a pipe geometry are limited to core–annular flow and side-by-side flow (Beckett et al., 2011). However, self-evidently, fissure eruptions are not fed by cylindrical conduits, but are fed by dykes, which are planar, crack-like features. We present the first scaled experimental study to investigate convective exchange flow in a dyke.

2. Methods and materials

2.1. Experimental materials

2.1.1. Fluid viscosity

Rotational rheometry was used to characterize the viscosity of the Newtonian working fluids used in this study: golden syrup, diluted golden syrup, glycerol and rapeseed oil. The rheological characterization was performed on a TA instruments Discovery Hybrid HR2 rheometer at Durham University, using a cone and plate measuring geometry with temperature control (Peltier plate). A solvent trap, filled with deionized water, was used to minimize dehydration during rheometry. Using TA instruments' Trios software, the rheometer and sensor system were calibrated for internal friction, thermal expansion and inertia at the start of the measurement campaign, and for each subsequent measurement the measuring geometry was calibrated for any precession upon rotation. Each time a new aliquot of sample was loaded, it was left for 10 minutes to reach thermal equilibrium with the Peltier plate.

During the rotational rheometry the flow curve (shear stress as a function of shear strain-rate) was determined over the strain-rate interval 0.01 s^{-1} to 100 s^{-1}, with 10 measurement points per decade, distributed logarithmically. Using this experimental approach, the viscosities of the working fluids were determined at temperatures: 10 °C, 14 °C, 18 °C, 20 °C, 22 °C, 26 °C and 30 °C in order to bracket the range of lab temperatures recorded during exchange experiments. For some fluids an additional set of measurements were taken at 21 °C to improve the data quality. To quantify the measurement error, the fluid that showed the most variability (oil) during the rheometry was measured three times, across the full temperature range. After calculation of viscosity from the flow curve, the largest 1σ was 8%. This is taken to be the maximum uncertainty for a given measurement incorporating machine errors and slight sample under- and over-filling in the rheometer.

Table 1
The viscosity fitting parameters for working fluids used in this study (Eq. 1). Cold pure golden syrup (cPGS) and pure golden syrup (PGS) are the same fluid but used at different temperatures (approximately 18 °C and 22 °C respectively). The exact fluid temperature was measured immediately after each experiment and was used to calculate the viscosity of the fluids for that experiment. The viscosity of air was assumed to be 2 x 10^{-5} Pa s.

Fluid	μ_0 [Pa s]	k [°C^{-1}]	R^2
cPGS & PGS	1859.2	0.168	0.99162
DGS	359.18	0.173	0.96133
gly	14.993	0.133	0.96971
oil	0.1905	0.046	0.98627

Table 2
The density fitting parameters for working fluids used in this study (Eq. 2). Cold pure golden syrup (cPGS) and pure golden syrup (PGS) are the same fluid but used at different temperatures (approximately 18 °C and 22 °C respectively). The exact fluid temperature was measured immediately after each experiment and was used to calculate the density of the fluids for that experiment. The density of air was assumed to be 1.2 kg m^{-3}.

Fluid	A [kg m^{-3} °C^{-1}]	B [kg m^{-3}]	R^2
cPGS & PGS	−0.5593	1450.1	0.9799
DGS	−0.5872	1420.0	0.9898
gly	−0.6104	1272.0	0.9980
oil	−0.6699	929.48	0.9992

All working fluids showed Newtonian rheology at all temperatures. The temperature dependence of viscosity $\mu(T)$ is best approximated by the following general form:

$$\mu = \mu_0 e^{-kT} \tag{1}$$

where μ_0 [Pa s] is the viscosity at 0 °C, T [°C] is the temperature and k [°C^{-1}] is an empirical exponent. Table 1 presents these parameters for each fluid.

2.1.2. Fluid density

The densities of the working fluids were measured using a calibrated 50 ml pycnometer flask. Fluids were added to the flask and left to equilibrate at 10, 12, 14, 16, 18, 20, 22, 24, 26, 28 and 30 °C within a temperature-controlled water bath. Once equilibrated, the flask exterior was dried and its mass measured on a ±500 µg desktop balance.

Over the temperature range investigated (10–30 °C), the density of a particular fluid follows the purely empirical general expression:

$$\rho = AT + B \tag{2}$$

where T [°C^{-1}] is the temperature and A [kg m^{-3} °C^{-1}] and B [kg m^{-3}] are constants. Table 2 presents these parameters for each fluid.

2.1.3. Experimental methods

The experimental apparatus used in this study comprises two cuboidal reservoirs (∼ 0.03 m^3 each) connected by a 2 m long, 1 m high slot with an internal gap width (D) of 0.02 m. The slot walls are made from transparent 15 mm thick acrylic panels to allow observation of flow patterns. Several metal support braces

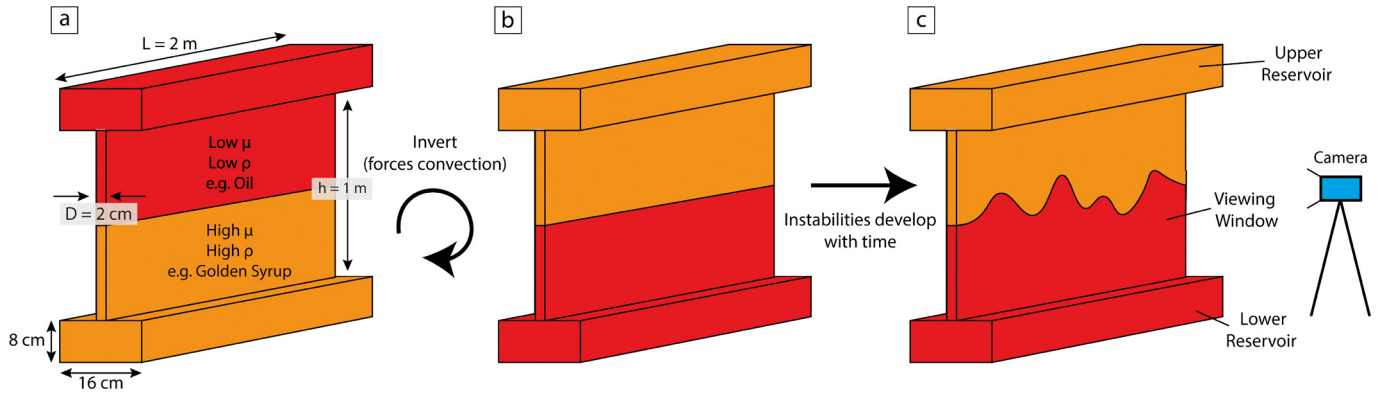

Fig. 2. The experimental apparatus used in this study and an abbreviated methodology. **(a)** Initial set-up of the high aspect ratio tank where a high density, high viscosity fluid is stratified below a fluid of lower density and viscosity. **(b)** The apparatus is then inverted 180° to initiate convection. **(c)** Instabilities and exchange flow develop, and concurrent filming is used for subsequent quantitative image analysis.

minimize deformation of the slot once fluid is added. The apparatus is suspended above the ground by a metal frame allowing for a full 360° rotation about its long axis (Fig. 2). In each experiment, the apparatus was initially half filled with a working fluid and left to settle (allowing bubbles introduced during filling to escape). Then, a second working fluid with lower density and viscosity was slowly added until the apparatus was full. The apparatus was sealed, checked for leaks and/or trapped gas pockets, then left for a few minutes until, by visual inspection, the interface between the two fluids was undisturbed and horizontal. A Nikon D7200 DSLR camera was positioned 2.7 m away from the apparatus, perpendicular to a slot wall, and set to acquire 2 images every 2 seconds; a timer was placed in the field of view. The specific camera settings that yielded the best images under our laboratory conditions were: 2000 ISO, 1/250 shutter speed, and f/4 aperture. The kit was inverted by 180° to initiate exchange. The first image after inversion was defined as the experiment start time (t_0). The end of the experiment (t_{end}) was defined as the time at which the lower density, lower viscosity fluid began to fill the slot from the upper reservoir (i.e. when parts of the upper reservoir became full). Lastly, the apparatus was inverted again, back to its original position and the temperature of the internal fluid was measured using a calibrated thermocouple. This temperature was used to calculate the fluid viscosity and density using empirical equations presented in Section 2.1.

This procedure was conducted at least five times for each of the following fluid combinations: cold pure golden syrup (cPGS) and air; pure golden syrup (PGS) and air; PGS and oil; diluted golden syrup (DGS) and oil; glycerol (gly) and oil. After the experiments using a specific fluid pairing were completed, an aliquot of each was taken and the viscosity and density were determined as functions of temperature.

In order to quantify any deformation of the slot arising from the hydrostatic pressure of the working fluids, the apparatus was filled with water and the window deflection measured at six places across the tank at 10 cm vertical intervals. The slot retains a 2 cm width at the very top and bottom of the apparatus where it is connected to the reservoirs but deforms slightly elsewhere. The average deformation of each window was 0.3 cm at 10 cm depth, 0.6 cm at 20 cm depth and $\sim$ 1 cm ($\pm$ 0.2 cm) thereafter. Although these gap width variations may have some influence on the flow patterns within the slot, the fixed gap width of the top and bottom of the slot, where it is connected to the reservoirs, is expected to be the dominant geometric control on the exchange flux for all experiments. One further source of uncertainty in D arises from the presence of a thin film of the more viscous fluid that coats the walls of the slot after the first inversion, thereby slightly reducing D. From visual inspection during the experiments we estimate this film to be $\leq$ 1 mm. It is always the more viscous fluid that coats the walls, which means that it does not have a lubricating effect on the flow, hence its only impact on exchange flux measurements is through effective narrowing of the gap by $\leq$5%. These gap width errors are systematic and remain near constant for all experiments. The random error associated with tracing, material characterization and experimental variability is reported as error bars on all figures.

2.2. Image analysis methods

The fluid flow patterns observed during the experiments typically feature the following series of events: (1) the initial development of an instability at the interface; (2) the growth and/or decay of upwelling fingers, and (3) steady state exchange flow. These processes were quantified via image analysis using a graphics package (Inkscape or Adobe Illustrator). To aid comparison of the experiments, the timestamp on the image of interest, t_{mea} was converted to a dimensionless time (t^*) – i.e. the elapsed time as a fraction of the total experimental time:

$$t^* = \frac{t_{mea} - t_0}{t_{end} - t_0}. \quad (3)$$

Firstly, the volume of lower viscosity, lower density fluid above the initial interface line was measured for three experiments from each fluid combination at multiple (11–13) time points between t_0 and t_{end}, to track the exchanged volume over time. To do this, the starting image at t_0 (with the horizontal interface line) was overlain on the image to be measured. Then, a reference interface line was drawn and all upwelling fluid within the slot, above this reference line, was traced to produce a binary mask. The area of the binary mask was then measured in ImageJ and, by assuming the fluid occupied the entire slot width (2 cm), converted to a volume of upwelling fluid. For images at longer times, after the upwelling fluid had reached the upper reservoir, an additional step was required to account for the volume held within the upper reservoir. The fluid area within the upper reservoir was measured in ImageJ and converted to a volume using the known reservoir dimensions. The sum of the slot volume and the upper reservoir volume provided the volume of lower viscosity fluid above the initial interface at a specific time within an experiment.

Secondly, the time-averaged volumetric flow rate Q [m^3 s^{-1}] was determined for every experiment. For each experiment, the final image (i.e. the image at t_{end}) was selected and any remaining denser, higher viscosity fluid area in the upper reservoir was measured using ImageJ. The area was then converted to a volume using the known reservoir dimensions. This volume was then subtracted from the total upper reservoir volume to give a volume change.

Then, the time-averaged volumetric flow rate was calculated by simply dividing this volume change (i.e. the emptying of the reservoir) by the time taken. Specifically, the time taken was calculated as $t_{end} - t_{up}$, where t_{up} is the time at which the upwelling fluid reaches the top reservoir. Furthermore, t_{up} is the time after which the flow dynamics are no longer confined to the slot, and fluid exchanges between the reservoirs. In all cases, the time-averaged volumetric flow rate, Q, was used in our calculations.

Finally, for one cPGS-air and one gly-oil experiment, the change in length of the interface between the two fluid phases was determined as a function of time during flow development (at $t^* =$ 0, 0.05, 0.25, 0.45, 0.65 and 0.85). The contact between all the upwelling and the co-existing downwelling fluid observed through the viewing window was traced. Then, the contact line was exported at a 1 pixel thickness and measured for area using ImageJ. Since the line was 1 pixel thick, the line area in pixels is equal to its length in pixels; using the scale bar, the distance in pixels was converted to meters.

3. Results and analysis

3.1. Description of flow evolution

Following inversion of the experimental apparatus, Rayleigh–Taylor instabilities develop at the interface between the fluids. The instabilities grow and organize into diverse flow patterns that depend on the viscosity of the downwelling fluid; typical sequences of this start-up flow are shown in Fig. S1, but are not the focus of this study. Once the upwelling fluid reaches the upper reservoir, an approximately steady-state exchange flow is set up between the two reservoirs until they are exhausted (Supplementary Videos 1–4). For experiments that use cold pure golden syrup and air (cPGS–air), or pure golden syrup and air (PGS–air), steady-state exchange is characterized by one, or sometimes two, narrow finger(s) of rapidly upwelling fluid separating broader regions of slowly downwelling fluid (Fig. 3). The PGS–oil experiments show a similar steady-state configuration, but follow a more complex flow evolution, in which some fingers bifurcate and form multi-lobed heads during ascent. The experiments that use diluted golden syrup and oil (DGS–oil) are much more dynamic: as the fingers grow they coalesce, bifurcate and re-join. Although these DGS–oil experiments feature multiple upwelling fingers that readily bifurcate and migrate through time, well-defined regions of ascending and descending fluid still develop. The experiments that use glycerol and oil (gly–oil) do not develop upwelling and downwelling fingers, but display chaotic, unorganized exchange flow. Throughout exchange, the flow comprises disconnected packets of rapidly-moving rising and descending fluid, and there are no persistent loci of upwelling or downwelling. A list of experiments and results can be found in Table S1.

3.2. Exchange flux

The volume of the upwelling fluid above the initial interface line, determined according to the methodology presented in Section 2.2, is plotted as a function of time in Fig. 4. For all experiments the volume increases linearly with time, hence volumetric flux is constant. The flux determined from the gradient of the volume–time curves in Fig. 4b is in close agreement with the time-averaged volumetric flow rate Q (Table S1) indicating that exchange flux remains approximately constant throughout the experiment.

3.3. The fluid dynamics of convective exchange flow

Exchange flow is governed by the Grashof number (Beckett et al., 2011; Huppert and Hallworth, 2007; Palma et al., 2011):

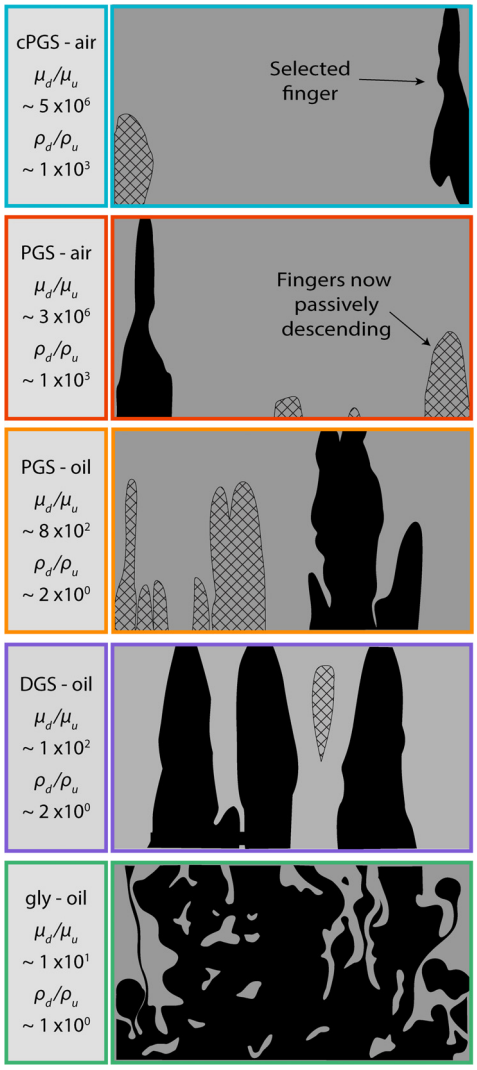

Fig. 3. Binarized images from quasi-steady-state exchange flow experiments (start-up flow is not considered in this study): cold PGS – air (blue); PGS – air (red); PGS – oil (orange); DGS – oil (purple) and gly – oil (green) experiments at $t^* = 0.85$. In each image the black and grey colors represent the upwelling fluid and the downwelling respectively. Cross-hatched markings represent lower density, lower viscosity fluid that was previously upwelling but is now passively descending, carried by the more-viscous fluid. Viscosity (μ) and density (ρ) ratios are shown for the fluid pairings. Where the subscripts u and d represent the upwelling and downwelling fluids respectively. (For interpretation of the colors in the figure(s), the reader is referred to the web version of this article.)

$$\mathrm{Gr} = \frac{\rho_d \, \Delta\rho g D^3}{\mu_d^2}; \tag{4}$$

where the subscripts u and d represent the upwelling and downwelling fluids respectively, ρ [kg m^{-3}] is fluid density, $\Delta\rho = \rho_d - \rho_u$, g [m s^{-2}] is gravitational acceleration, D [m] is the width of the slot (diameter for the pipe case), and μ [Pa s] is fluid viscosity. The downwelling fluid viscosity, μ_d was always used in the calculation for Gr because in our experiments $\mu_d \gg \mu_u$ and the most viscous fluid is known to dominate the system behavior (Huppert and Hallworth, 2007). The Grashof number is an intrinsic property of the convecting system, which includes only material and geometric parameters; i.e., no parameters must be determined from the exchange experiments. It therefore represents the independent variable and is particularly useful because it can be straightforwardly estimated for volcanic systems.

The dependent variable in the convecting system is the exchange flux Q (volume per time). In the general case, the exchange

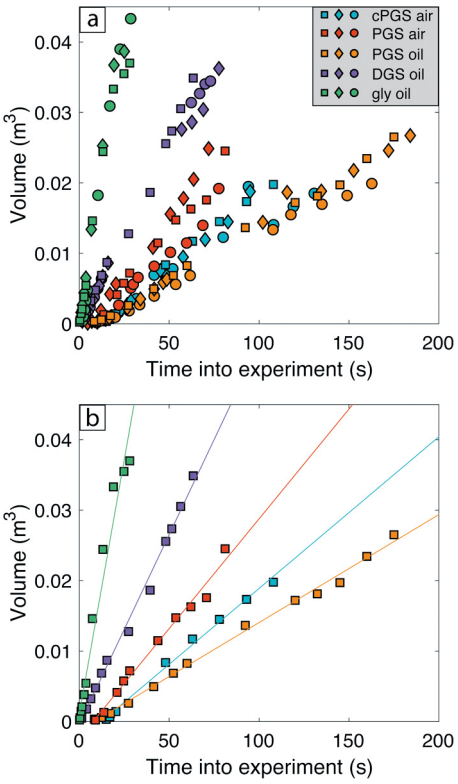

Fig. 4. The volume of the upwelling fluid above the initial interface line shown as a function of time into the experiment. **(a)** All results from three different repeat experiments (denoted by symbol shape) of each different fluid combinations (denoted by the symbol color). **(b)** One experiment for each fluid pairing is re-plotted and a linear regression fitted; the gradient gives the volumetric flow rate [$m^3\ s^{-1}$]. 1σ error bars are smaller than the data points.

flux is given by $Q = \min(|Q_u|, |Q_d|)$ where $\min(-,-)$ represents the smaller of the two quantities and Q_u and Q_d represent the upwelling and downwelling volume fluxes respectively. For our experiments, $Q = |Q_u| = |Q_d|$. We non-dimensionalize the exchange flux against the flux with which the downwelling fluid would drain from the slot under reduced gravity ($\Delta\rho g/\rho_d$) assuming Hagen–Poiseuille flow (Q_{HP}):

$$Q^* = \frac{Q}{Q_{HP}} = \frac{12\mu_d Q}{\Delta\rho g D^3 L}; \tag{5}$$

where L is the length of the slot. We term this parameter the 'exchange efficiency', and we expect that $Q^* \leq 1$ because the exchange flux should not be greater than the Hagen–Poiseuille drainage flux. We note that Q^* is cognate with the 'transport number' that was developed by Huppert and Hallworth (2007) to describe exchange efficiency in a pipe, but has the advantage that its physical meaning is evident.

Fig. 5 shows these two dimensionless parameters for our experiments and we can determine a quantitative relationship for $Q^*(\mathrm{Gr})$. For $\mathrm{Gr} < 0.1$ we find that the exchange efficiency is independent of Grashof number; for $\mathrm{Gr} > 0.1$ we find that exchange efficiency decreases systematically with increasing Grashof number. This is consistent with the observations of Huppert and Hallworth (2007), who find an exponential decrease in transport number (cognate with Q^*) with increasing Reynolds number (cognate with Gr) for exchange in a cylindrical pipe. Our form has the physically-desirable property that it asymptotes to zero exchange efficiency at high Gr. We fit an exponential function to the data for $\mathrm{Gr} > 0.1$, giving the following relationships for $Q^*(\mathrm{Gr})$:

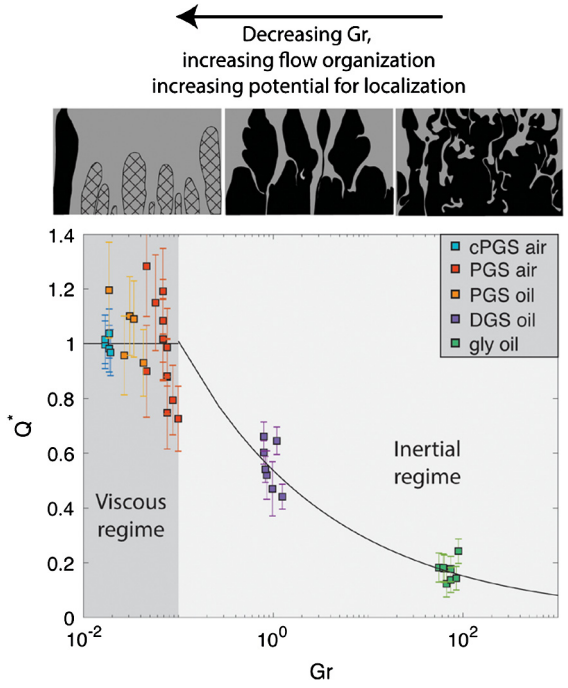

Fig. 5. The exchange efficiency (Q^*) as a function of Grashof number (Gr) for all experiments. Error bars on data points show the 1σ compound error. The dark and light grey shading mark the viscous and inertial regimes respectively. Following Huppert and Hallworth (2007), we fit an exponential function to the data in the high Grashof number regime (Eq. 6), whereas in the low Grashof number (viscous) regime $Q^* = 1$.

$$Q^* = \begin{cases} 1 & : \mathrm{Gr} \leq 0.1 \\ 0.537\,\mathrm{Gr}^{-0.274} & : \mathrm{Gr} > 0.1 \end{cases} \tag{6}$$

Furthermore, in combination with Equation (5), this allows us to calculate exchange flux per unit slot length as:

$$\frac{Q}{L} = \begin{cases} \frac{\mu_d \mathrm{Gr}}{12\,\rho_d} & : \mathrm{Gr} \leq 0.1 \\ 0.0448\,\frac{\mu_d \mathrm{Gr}^{0.726}}{\rho_d} & : \mathrm{Gr} > 0.1 \end{cases} \tag{7}$$

3.4. Scaling between experiments and the natural system

In both the experiments and the natural system, the fully developed flow is characterized by convective exchange of fluids with different densities and viscosities. Our experiments are designed such that they overlap the same range of the controlling dimensionless parameter Gr as found in nature (Table 3).

The development of the flow is captured in the evolution of the total length of fluid interface in the apparatus as a function of time: plots for $\mathrm{Gr} \approx 10^{-2}$ and $\mathrm{Gr} \approx 10^{2}$ are presented in Fig. 6. At low Gr the total length of the interface increases rapidly after flow onset, as multiple fingers form, but then decays monotonically as the number of fingers drops (Fig. 6; Fig. S1). This demonstrates that the well-organized developed flow configuration of the low Gr system establishes despite a poorly-organized configuration during start-up flow – i.e. perturbations tend to decay as flow becomes developed. By contrast, at high Gr the total length of the interface remains high throughout start-up and fully developed flow because blebs of both fluids divide and coalesce continuously and chaotically. This implies that even a well-organized initial condition would undergo chaotic bifurcation of the fingers that would rapidly lead to poor organization. Consequently, we conclude that the developed flow behavior that we observe in our experiments is not an artefact of the initial conditions.

The fluids used in our experiments are immiscible, hence the interface between the fluids is subject to surface tension; this dif-

Table 3
Parameter values for both natural eruptions (gathered from the literature) and the experiments. Natural density estimates for basaltic melt derive from (Jones et al., 2018; Murase and McBirney, 1973). Natural dyke width and length estimates derive from (Parcheta et al., 2015; Thorarinsson and Sigvaldason, 1962). Basaltic viscosity estimates derive from (Giordano et al., 2008; Giordano and Dingwell, 2003). An interfacial tension of 0.08 N m^{-1} was used for the (c)PGS – air experiments (Llewellin et al., 2002) and, due to limited data availability, an approximate interfacial tension of 0.03 N m^{-1} (measured for oil against water) for the experiments that use oil as the low viscosity fluid (Fisher et al., 1985; Gaonkar, 1989).

	Units	Symbol	Nature	Experiment
Descending fluid density	kg m^{-3}	ρ_d	2200	1440 (cPGS) to 1260 (gly)
Upwelling fluid density	kg m^{-3}	ρ_u	900	914 (oil) to 1.2 (air)
Density difference	kg m^{-3}	$\Delta\rho$	1300	1440 (cPGS – air) to 345 (gly – oil)
Crack/slot length	m	L	40 to 6000	2
Crack/slot width	m	D	0.5 to 3	0.02
Descending fluid viscosity	Pa s	μ_d	10^3 to 10^1	95 (cPGS) to 0.9 (gly)
Upwelling fluid viscosity	Pa s	μ_u	10^3 to 10^1	0.07 (oil) to $2x10^{-5}$ (air)
Surface tension	N m^{-1}	σ	0	0.08 to 0.03
Gravity	m^2 s^{-1}	g	9.81	9.81
Grashof Number		Gr	10^{-3} to 10^4	10^{-2} to 10^2

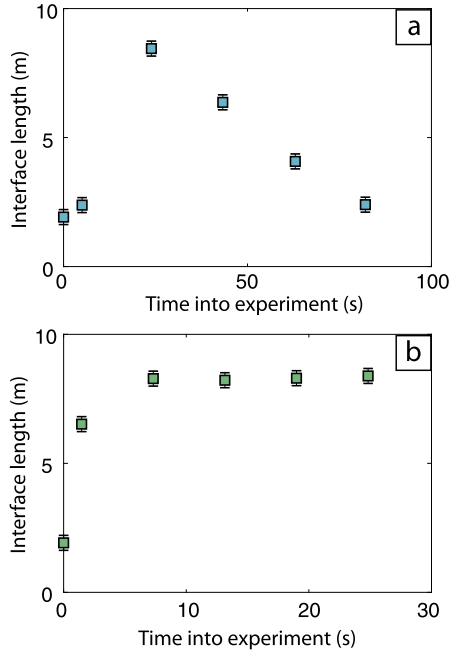

Fig. 6. The total length of the interface between the upwelling and downwelling fluids as a function of time during start up flow. **(a)** For cPGS – air ($Gr \approx 10^{-2}$) the total length of the interface climbs rapidly as fingers grow, then decays over time as the number of fingers decreases monotonically until flow is fully developed. **(b)** For gly – oil ($Gr \approx 10^2$) the total length of the interface climbs rapidly as fingers grow and bifurcate. Sustained bifurcation leads to a large number of chaotically interacting blebs of each fluid, which persist throughout fully developed flow, hence the total interface length remains high.

fers from the natural system, in which the ascending and descending magmas are assumed to be miscible. Previous studies (Chang, 1959; Mikaelian, 1990) have shown that the primary effect of surface tension on Rayleigh-Taylor instabilities is to introduce a cut off wavelength, $\lambda_c = 2\pi/\sqrt{(\rho_d - \rho_u)\, g/\sigma}$, where σ is the surface tension between the two fluids. Instabilities with wavelength $\lambda < \lambda_c$ are suppressed by surface tension, whereas instabilities with wavelength $\lambda > \lambda_c$ are stable and may grow. λ_c is 1.5 cm, 1.5 cm, 1.5 cm, 1.6 cm, and 1.9 cm for the cPGS – air, PGS – air, PGS – oil, DGS – oil and gly – oil experiments respectively (cf. Table 3). In all our experiments, across all Gr, the observed wavelengths (Videos S1–4) of both developing instabilities and developed flow patterns are longer than λ_c, indicating that surface tension does not play a role in determining the development of the fluid dynamic phenomena, or their observed variation with Gr. This implies that flow patterns are set by the hydrodynamics of the system, rather than surface tension; hence our experiments are a valid analogue for exchanging magmas despite the difference in miscibility.

4. Discussion

4.1. Fluid flow patterns in the sub-volcanic plumbing system

Exchange flow in a slot shows much greater richness of fluid dynamic phenomena than has been described in a cylindrical pipe (Beckett et al., 2011). We contend that flow in a slot provides a much stronger experimental analogy for flow in natural basaltic conduits. The flow patterns observed in this study show a systematic dependence on Grashof number. Experiments at low Grashof number ($Gr \lesssim 0.1$) form well-organized channels, those at intermediate Grashof number ($Gr \sim 1$) form bifurcating channels that may migrate laterally over time, and those at the highest Grashof number ($Gr \sim 100$) are chaotic, characterized by interacting blebs of upwelling and downwelling liquid. We find that the exchange efficiency generally decreases with increasing Grashof number (Fig. 5). We attribute this to the decreasing degree of flow pattern organization and the hindering effect of bleb interaction as Grashof number increases.

The experiments can be organized into two regimes based on exchange flow pattern and exchange efficiency. For $Gr < 0.1$, flow is well-organized and exchange efficiency is approximately $Q^* = 1$. Some individual data points lie at $Q^* > 1$, but the mean value of Q^* for each of the experimental suites in this regime (cPGS – air, PGS – oil, PGS – air) is very close to unity, and the best fit straight line through these data points is within error of $Q^* = 1$. For $Gr > 0.1$, flow is increasingly chaotic and exchange efficiency decreases with increasing Grashof number. Grashof number describes the balance between viscous and inertial forces arising from buoyancy; in the low Grashof number regime viscous forces dominate, and in the high Grashof number regime inertial forces dominate; hence, we use the terms 'viscous regime' and 'inertial regime' for $Gr < 0.1$ and $Gr > 0.1$ respectively.

For the volcanic case, the dominant controls on the Grashof number are the dyke width and the viscosity of the descending magma. In general, the effective dyke width is expected to decrease in the early part of an eruption as magma accretes to the cold walls (Bruce and Huppert, 1989; Delaney and Pollard, 1982), and the viscosity of the descending magma is likely to increase through a combination of degassing, crystallization (particularly of microlites), and cooling (Giordano and Dingwell, 2003; Mader et al., 2013). Both changes act to decrease the Grashof number, so exchange flow of magma in a dyke is expected to become less chaotic and more organized over time.

4.2. A 'tipping point' for eruption localization

Evolution of the flow regime in the sub-volcanic dyke has important implications for the localization of a fissure eruption. Localization is a result of thermal (Bruce and Huppert, 1989) and thermo-rheological (Wylie et al., 1999) feedbacks. Slight temperature perturbations along-strike induce variations in magma viscosity which cause flow to focus in regions of lowest viscosity – i.e. viscous fingering (Helfrich, 1995; Wylie et al., 1999). Using this existing framework in tandem with our new experimental results, we propose that a shift in the convective flow regime (and therefore subsurface flow patterns) acts as a 'tipping point' between conditions that hinder or enhance fissure localization via thermal and thermo-rheological feedbacks. Initially, eruptions have high Grashof number and exhibit chaotic, poorly organized subsurface convective flow in which the descent of dense, degassed magma disrupts the ascent of buoyant, fresh magma (Fig. 5). The resultant chaotic mingling dampens along-strike thermal gradients; hence, in this inertial flow regime, the formation of low viscosity fingers is hindered, and thermo-rheological localization is suppressed (Fig. 7a). Over time, increasing magma viscosity (through cooling and crystallization) and/or decreasing effective dyke width decrease the Grashof number until convective flow transitions to the viscous regime ($\mathrm{Gr} \leq 0.1$). Well organized convective exchange in this regime enhances the development of along-strike thermal gradients, facilitating stable viscous fingering (Fig. 7b). This flow pattern induces along-strike variations in velocity and heat advection, supporting fissure localization. We suggest that the regime divide between chaotic inertial behavior and organized viscous fingering acts as a critical tipping point – only when an eruption transitions into the viscous regime can along-strike thermal gradients develop sufficiently to initiate localization. Furthermore, eruptions that spend longer in the high Grashof number regime are expected to take longer to localize.

4.3. Model illustration for a basaltic fissure eruption

To further illustrate our conceptual model for basaltic fissure localization we consider a typical Hawaiian fissure eruption and its associated temporal evolution. We take the dyke width as $D = 1$ m, which is typical of Kīlauea (Parcheta et al., 2015), and estimate density based on an analogy with bulk density measurements made by Jones et al. (2018) on products from the 1969 Mauna Ulu basaltic fissure eruption. For that eruption, "primary spatter", which is the most juvenile material was taken to represent the upwelling magma and has a vesicularity of 63%; "late-stage spatter", which is the most mature material, was taken to represent the downwelling magma, and has a vesicularity of 49%. The temperature of the erupting magma is taken to be 1150 °C, which is typical for Kīlauea (Chevrel et al., 2018; Pinkerton et al., 2002; Swanson et al., 1979). The density of the bubble-free melt is calculated as 2745 kg m^{-3} using a typical Kilauea basalt composition (Chevrel et al., 2018; Lesher and Spera, 2015), giving $\rho_u = 1015$ kg m^{-3} and $\rho_d = 1400$ kg m^{-3}, hence $\Delta\rho = 385$ kg m^{-3}, when vesicularity is taken into account. The viscosity of the melt is calculated (Giordano et al., 2008) as $\mu_l = 293$ Pa s. The impact of bubbles and crystals on viscosity is calculated following Truby et al. (2015), assuming that the crystals are microlites, which are much smaller than the bubbles:

$$\mu = \mu_l (1 - \phi_b)^{-1} \left(1 - \frac{\phi_c}{\phi_m}\right)^{-2} \tag{8}$$

where the volume fraction of bubbles, $\phi_b = 0.49$ for downwelling magma, ϕ_c is the volume fraction of microlite crystals in the melt phase, and ϕ_m is the maximum packing fraction of crystals. This is estimated from the aspect ratio of the crystals r_p which is approximately 10 for microlites in basalt (Applegarth et al., 2013), via the relationship $\phi_m = 0.55 \exp\left(-\log_{10} r_p^2/2\right)$ from Mader et al. (2013). We check that bubbles are in the low capillary number regime ($\mathrm{Ca} < 1$ where $\mathrm{Ca} = \mu_l a \dot{\gamma}/\sigma$, a is bubble radius, $\dot{\gamma}$ is the strain rate, and σ is the surface tension) by calculating exchange flux per unit length, from Equation (7), and considering the typical strain rate in the dyke as: $\dot{\gamma} = Q/LD^2$. For conservative values of bubble radius ($a = 1$ mm) and surface tension ($\sigma = 0.2$ N/m), $\mathrm{Ca} < 1$ for all cases considered, hence the Truby et al. (2015) analysis is valid.

For the initial opening phase of the fissure eruption, we assume that $\phi_c = 0$, hence the viscosity of the downwelling magma is $\mu_d = 577$ Pa s, giving a Grashof number of $\mathrm{Gr} = 16$. This is well into the chaotic regime (cf. Fig. 5) and, in order to reach the tipping point, the Grashof number needs to decrease by a fac-

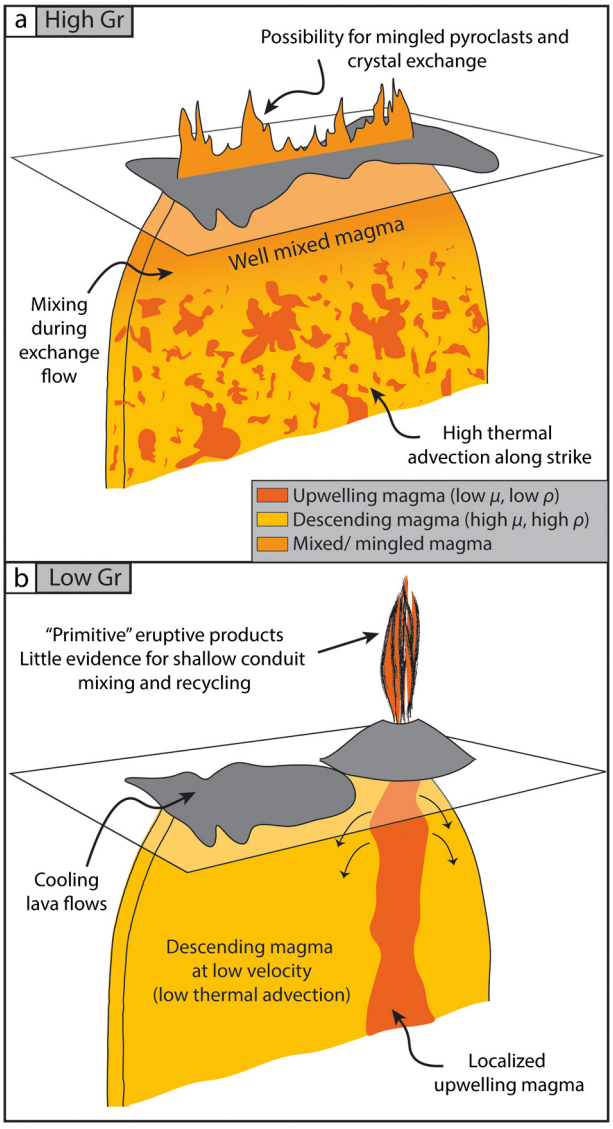

Fig. 7. The subsurface exchange flow dynamics at **(a)** high Gr and **(b)** low Gr. In the inertial regime at high Gr the exchange flow is chaotic with high thermal advection all along strike. This dampens any along-strike temperature perturbations and therefore hinders localization by thermo-rheological processes. In the viscous regime at low Gr the exchange flow is well organized into high velocity upwelling fingers and low velocity downwelling regions. This flow configuration creates large temperature perturbations along strike which are readily exploited by thermo-rheological localization processes. The flow is further focused into the upwelling region of high temperature, low viscosity.

tor of approximately 100, to Gr < 0.1. This can easily be achieved through a combination of increasing magma viscosity (e.g. temperature reduction, microlite crystallization) and decreasing dyke width. For example, one such combination is the growth of 15% by volume of acicular microlites ($\phi_c = 0.15$, giving $\mu_d = 2823$ Pa s), combined with cooling by 20 °C, and a 40% reduction in dyke width ($D = 0.6$ m). These changes are slight over the course of an eruption and can therefore readily produce the requisite decrease in Grashof number.

4.4. Other factors that influence eruption localization

There are other factors that may influence flow focusing and vent localization, in addition to the thermo-rheological processes (Bruce and Huppert, 1990, 1989; Helfrich, 1995; Moreland et al., 2019; Whitehead and Helfrich, 1991; Wylie et al., 1999) and convective flow patterns considered so far. One such factor is the spatial variation (especially along-strike variation) in magma properties or dyke width (e.g. Beckett et al., 2014; Ida, 1992; Mitchell, 2005; Parcheta et al., 2015). Where these quantities (width, viscosity, density) vary over a lengthscale that is much longer than the lengthscale of the relevant flow features – chaotic blebs, ascending and descending fingers – we would expect that the conceptual framework that we develop is still applicable, but that Gr will also vary spatially along with the dyke geometry and magma properties. Where the variation is over a lengthscale that is much shorter than the fluid dynamic lengthscale, we again expect that the conceptual framework is applicable, and that spatially-averaged quantities are applicable. Where the variation is over a lengthscale that is similar to the fluid dynamic lengthscale, there are likely to be complex interactions that defy simple analysis.

4.5. Further implications of exchange flow regimes

The flow regime and associated flow pattern has implications beyond flow localization (Fig. 7). Magma transport at high Grashof number is expected to be poorly organized, with abundant, chaotic interaction between blebs of upwelling and downwelling magma (Fig. 7a); consequently, enhanced mingling and modification of upwelling magma is expected, and crystals may show evidence for hybridization between fresh and degassed magma. By contrast, exchange flow in the viscous regime (Gr ≤ 0.1) would organize into well-defined upwelling channels, with limited interaction with the adjacent downwelling magma (Fig. 7b). Consequently, the upwelling magma would remain relatively unmodified through ascent. Crystals may show strong zonation, evidencing convection through the whole system before being recycled into the fresh magma at depth (Francalanci et al., 2012). The exchange flux is related to the Grashof number (Eq. 7) providing the potential for the Grashof number to be estimated for specific, monitored eruptions from measurements of excess gas. Assessing the eruption Grashof number in real-time could allow the evolution of a fissure eruption towards the localization tipping point to be tracked, providing a useful hazard monitoring tool.

5. Summary

We present the first quantitative model for exchange flow in basaltic dykes. Our experiments show that flow behavior in a dyke is phenomenologically much richer than in a cylindrical pipe, featuring convective regime transitions and along-strike organization of flow patterns that have not previously been described. The Grashof number determines the flow regime and associated convective patterns and characterizes a tipping point that leads to fissure localization. Exchange flow at low Grashof number, in the viscous regime, is characterized by narrow, well organized regions of upwelling separated by broader, lower velocity regions of downwelling. This flow configuration induces and enhances temperature perturbations along strike which are readily exploited by thermo-rheological localization processes. A positive feedback occurs, and the flow is further focused into the hotter, narrow upwelling region. In contrast, exchange flow at high Gr, in the inertial regime, is chaotic and unorganized with equal thermal advection along strike. This flow pattern supresses temperature perturbations and thus hinders vent localization. Our results introduce new fluid dynamic phenomena that operate in basaltic fissure eruptions, requiring that current conceptual, physical and numerical models of fissure eruptions and their evolution need to be revised.

CRediT authorship contribution statement

T.J. Jones: Conceptualization, Methodology, Experiments, Formal analysis, Data curation, Writing - original draft, Visualization. **E.W. Llewellin**: Conceptualization, Methodology, Resources, Writing - review & editing, Supervision, Visualization.

Declaration of competing interest

The authors declare that they have no known competing financial interests or personal relationships that could have appeared to influence the work reported in this paper.

Acknowledgements

TJJ acknowledges support from NERC grant NE/L002590/1. EWL acknowledges support from NERC grant NE/N018443/1. Laura Höltgen and Veronica Becker are thanked for their help with the experiments and image analysis respectively. The authors thank two anonymous reviewers whose comments helped improve this manuscript.

Appendix A. Supplementary material

Supplementary material related to this article can be found online at https://doi.org/10.1016/j.epsl.2020.116637.

References

Allard, P., Carbonnelle, J., Metrich, N., Loyer, H., Zettwoog, P., 1994. Sulphur output and magma degassing budget of Stromboli volcano. Nature 368, 326–330.
Applegarth, L.J., Tuffen, H., James, M.R., Pinkerton, H., Cashman, K.V., 2013. Direct observations of degassing-induced crystallization in basalts. Geology 41, 243–246.
Beckett, F.M., Burton, M., Mader, H.M., Phillips, J.C., Polacci, M., Rust, A.C., Witham, F., 2014. Conduit convection driving persistent degassing at basaltic volcanoes. J. Volcanol. Geotherm. Res. 283, 19–35.
Beckett, F.M., Mader, H.M., Phillips, J.C., Rust, A.C., Witham, F., 2011. An experimental study of low-Reynolds-number exchange flow of two Newtonian fluids in a vertical pipe. J. Fluid Mech. 682, 652–670.
Bruce, P.M., Huppert, H.E., 1990. Solidification and melting along dykes by the laminar flow of basaltic magma. In: Ryan, M.P. (Ed.), Magma Transport and Storage. Wiley, pp. 87–101.
Bruce, P.M., Huppert, H.E., 1989. Thermal control of basaltic fissure eruptions. Nature 342, 665–667.
Burton, M.R., Mader, H.M., Polacci, M., 2007. The role of gas percolation in quiescent degassing of persistently active basaltic volcanoes. Earth Planet. Sci. Lett. 264, 46–60. https://doi.org/10.1016/j.epsl.2007.08.028.
Chang, C.T., 1959. Dynamic instability of accelerated fluids. Phys. Fluids 2, 656–663.
Chevrel, M.O., Harris, A.J.L., James, M.R., Calabrò, L., Gurioli, L., Pinkerton, H., 2018. The viscosity of pahoehoe lava: in situ syn-eruptive measurements from Kilauea, Hawaii. Earth Planet. Sci. Lett. 493, 161–171.
Delaney, P.T., Pollard, D.D., 1982. Solidification of basaltic magma during flow in a dike. Am. J. Sci. 282, 856–885.
Fisher, L.R., Mitchell, E.E., Parker, N.S., 1985. Interfacial tensions of commercial vegetable oils with water. J. Food Sci. 50, 1201–1202.

Francalanci, L., Avanzinelli, R., Nardini, I., Tiepolo, M., Davidson, J.P., Vannucci, R., 2012. Crystal recycling in the steady-state system of the active Stromboli volcano: a 2.5-ka story inferred from in situ Sr-isotope and trace element data. Contrib. Mineral. Petrol. 163, 109–131.

Gaonkar, A.G., 1989. Interfacial tensions of vegetable oil/water systems: effect of oil purification. J. Am. Oil Chem. Soc. 66, 1090–1092.

Geshi, N., Neri, M., 2014. Dynamic feeder dyke systems in basaltic volcanoes: the exceptional example of the 1809 Etna eruption (Italy). Front. Earth Sci. 2, 13. https://doi.org/10.3389/feart.2014.00013.

Giordano, D., Dingwell, D., 2003. Viscosity of hydrous Etna basalt: implications for Plinian-style basaltic eruptions. Bull. Volcanol. 65, 8–14.

Giordano, D., Russell, J.K., Dingwell, D.B., 2008. Viscosity of magmatic liquids: a model. Earth Planet. Sci. Lett. 271, 123–134.

Helfrich, K.R., 1995. Thermo-viscous fingering of flow in a thin gap: a model of magma flow in dikes and fissures. J. Fluid Mech. 305, 219–238.

Houghton, B.F., Wilson, C.J.N., Del Carlo, P., Coltelli, M., Sable, J.E., Carey, R., 2004. The influence of conduit processes on changes in style of basaltic Plinian eruptions: Tarawera 1886 and Etna 122 BC. J. Volcanol. Geotherm. Res. 137, 1–14.

Huppert, H.E., Hallworth, M.A., 2007. Bi-directional flows in constrained systems. J. Fluid Mech. 578, 95–112.

Ida, Y., 1992. Width change of a planar magma path: implication for the evolution and style of volcanic eruptions. Phys. Earth Planet. Inter. 74, 127–138.

Jones, T.J., Houghton, B.F., Llewellin, E.W., Parcheta, C.E., Höltgen, L., 2018. Spatter matters – distinguishing primary (eruptive) and secondary (non-eruptive) spatter deposits. Sci. Rep. 8, 9179. https://doi.org/10.1038/s41598-018-27065-1.

Jones, T.J., Llewellin, E.W., Houghton, B.F., Brown, R.J., Vye-Brown, C., 2017. Proximal lava drainage controls on basaltic fissure eruption dynamics. Bull. Volcanol. 79, 81. https://doi.org/10.1007/s00445-017-1164-2.

Kazahaya, K., Shinohara, H., Saito, G., 1994. Excessive degassing of Izu-Oshima volcano: magma convection in a conduit. Bull. Volcanol. 56, 207–216.

Landi, P., Métrich, N., Bertagnini, A., Rosi, M., 2008. Recycling and "re-hydration" of degassed magma inducing transient dissolution/crystallization events at Stromboli (Italy). J. Volcanol. Geotherm. Res. 174, 325–336.

Lesher, C.E., Spera, F.J., 2015. Thermodynamic and transport properties of silicate melts and magma. In: Sigurdsson, H. (Ed.), The Encyclopedia of Volcanoes, second edition. Academic Press, Amsterdam, pp. 113–141. Chapter 5.

Llewellin, E.W., Mader, H.M., Wilson, S.D.R., 2002. The rheology of a bubbly liquid. Proc. R. Soc. Lond. A, Math. Phys. Eng. Sci., 987–1016.

Mader, H.M., Llewellin, E.W., Mueller, S.P., 2013. The rheology of two-phase magmas: a review and analysis. J. Volcanol. Geotherm. Res. 257, 135–158.

Mikaelian, K.O., 1990. Rayleigh-Taylor and Richtmyer-Meshkov instabilities in multilayer fluids with surface tension. Phys. Rev. A 42, 7211.

Mitchell, K.L., 2005. Coupled conduit flow and shape in explosive volcanic eruptions. J. Volcanol. Geotherm. Res. 143, 187–203.

Moreland, W.M., Thordarson, T., Houghton, B.F., Larsen, G., 2019. Driving mechanisms of subaerial and subglacial explosive episodes during the 10th century Eldgjá fissure eruption, southern Iceland. Volcanica 2, 129–150.

Murase, T., McBirney, A.R., 1973. Properties of some common igneous rocks and their melts at high temperatures. Geol. Soc. Am. Bull. 84, 3563–3592.

Oppenheimer, C., McGonigle, A.J.S., Allard, P., Wooster, M.J., Tsanev, V., 2004. Sulfur, heat, and magma budget of Erta 'Ale lava lake, Ethiopia. Geology 32, 509–512.

Palma, J.L., Blake, S., Calder, E.S., 2011. Constraints on the rates of degassing and convection in basaltic open-vent volcanoes. Geochem. Geophys. Geosyst. 12. https://doi.org/10.1029/2011GC003715.

Palma, J.L., Calder, E.S., Basualto, D., Blake, S., Rothery, D.A., 2008. Correlations between SO2 flux, seismicity, and outgassing activity at the open vent of Villarrica volcano, Chile. J. Geophys. Res., Solid Earth 113.

Parcheta, C., Fagents, S., Swanson, D.A., Houghton, B.F., Ericksen, T., 2015. Hawaiian Fissure Fountains: quantifying vent and shallow conduit geometry, Episode 1 of the 1969–1974 Mauna Ulu eruption. In: Hawaiian Volcanoes: From Source to Surface. John Wiley & Sons, Inc, p. 369.

Pinkerton, H., James, M., Jones, A., 2002. Surface temperature measurements of active lava flows on Kilauea volcano, Hawaii. J. Volcanol. Geotherm. Res. 113, 159–176.

Pioli, L., Azzopardi, B.J., Bonadonna, C., Brunet, M., Kurokawa, A.K., 2017. Outgassing and eruption of basaltic magmas: the effect of conduit geometry. Geology 45, 759–762.

Stevenson, D.S., Blake, S., 1998. Modelling the dynamics and thermodynamics of volcanic degassing. Bull. Volcanol. 60, 307–317.

Swanson, D.A., Duffield, W.A., Jackson, D.B., Peterson, D.W., Off, U.S.G.P., 1979. Chronological narrative of the 1969-71 Mauna Ulu eruption of Kilauea Volcano, Hawaii. US Geological Survey professional paper 1056.

Thorarinsson, S., Sigvaldason, G.E., 1962. The eruption in Askja, 1961, a preliminary report. Am. J. Sci. 260, 641–651.

Truby, J.M., Mueller, S.P., Llewellin, E.W., Mader, H.M., 2015. The rheology of three-phase suspensions at low bubble capillary number. Proc. R. Soc. A, 20140557.

Wadsworth, F.B., Kennedy, B.M., Branney, M.J., von Aulock, F.W., Lavallée, Y., Menendez, A., 2015. Exhumed conduit records magma ascent and drain-back during a strombolian eruption at Tongariro volcano, New Zealand. Bull. Volcanol. 77, 1–10. https://doi.org/10.1007/s00445-015-0962-7.

Whitehead, J.A., Helfrich, K.R., 1991. Instability of flow with temperature-dependent viscosity: a model of magma dynamics. J. Geophys. Res., Solid Earth 96, 4145–4155. https://doi.org/10.1029/90JB02342.

Wilson, L., Parfitt, E.A., Head, J.W., 1995. Explosive volcanic eruptions—VIII. The role of magma recycling in controlling the behaviour of Hawaiian-style lava fountains. Geophys. J. Int. 121, 215–225. https://doi.org/10.1111/j.1365-246X.1995.tb03522.x.

Witham, F., 2011. Conduit convection, magma mixing, and melt inclusion trends at persistently degassing volcanoes. Earth Planet. Sci. Lett. 301, 345–352.

Wylie, J.J., Helfrich, K.R., Dade, B., Lister, J.R., Salzig, J.F., 1999. Flow localization in fissure eruptions. Bull. Volcanol. 60, 432–440. https://doi.org/10.1007/s004450050243.